THE PHYSICS OF PROTOPLANETESIMAL DUST AGGLOMERATES. VI. EROSION OF LARGE AGGREGATES AS A SOURCE OF MICROMETER-SIZED PARTICLES

Rainer Schräpler and Jürgen Blum
Institut für Geophysik und extraterrestrische Physik, University of Braunschweig
Mendelssohnstr. 3, D-38106 Braunschweig, Germany; r.schraepler@tu-bs.de

ABSTRACT

Observed protoplanetary disks consist of a large amount of micrometer-sized particles. Dullemond & Dominik pointed out for the first time the difficulty in explaining the strong mid-infrared excess of classical T Tauri stars without any dust-retention mechanisms. Because high relative velocities in between micrometer-sized and macroscopic particles exist in protoplanetary disks, we present experimental results on the erosion of macroscopic agglomerates consisting of micrometer-sized spherical particles via the impact of micrometer-sized particles. We find that after an initial phase, in which an impacting particle erodes up to 10 particles of an agglomerate, the impacting particles compress the agglomerate's surface, which partly passivates the agglomerates against erosion. Due to this effect, the erosion halts for impact velocities up to ∼30 m s^{-1} within our error bars. For higher velocities, the erosion is reduced by an order of magnitude. This outcome is explained and confirmed by a numerical model. In a next step, we build an analytical disk model and implement the experimentally found erosive effect. The model shows that erosion is a strong source of micrometer-sized particles in a protoplanetary disk. Finally, we use the stationary solution of this model to explain the amount of micrometer-sized particles in the observational infrared data of Furlan et al.

Key words: methods: analytical – methods: laboratory – protoplanetary disks

Online-only material: color figures

1. INTRODUCTION

Early theoretical investigations concerning planet formation followed two paradigms. The first paradigm considers a laminar nebula in which dust particles coagulate as a result of Brownian motion and differential drift velocities. Most particles arriving at the midplane at 1 AU reach sizes of 1–10 cm within 1500–3000 orbits (Weidenschilling 1980; Nakagawa et al. 1981, 1986). This settling leads to a dust-dominated sub-disk, which remains a finite thickness owing to shear turbulence (Schräpler & Henning 2004; Cuzzi et al. 1993; Weidenschilling 2006, 1988, 1984, 1980). The shear turbulence is generated by the difference in orbital velocity between the pressure-supported gas disk and the dust-dominated sub-disk (Schräpler & Henning 2004; Cuzzi et al. 1993). In the sub-disk, particles can grow to large agglomerates (Schräpler & Henning 2004), whereas below and above the sub-disk a strong outward-directed wind is generated. This wind, which has typical velocities of 30 m s^{-1} at 1 AU (Weidenschilling 2006; Cuzzi et al. 1993), carries along small particles that are perfectly coupled to the gas.

The second paradigm considers a fully turbulent nebula. The dust within the disk coagulates due to random velocities provided by the turbulent gas motion (Brauer et al. 2008; Schmitt et al. 1997). The strong turbulent motion in the gas prevents the formation of a dust sub-disk. After the particles have coagulated to several decimeters in size, they begin to migrate inward with velocities up to 50 m s^{-1}, owing to friction with the sub-Keplerian gas disk (Weidenschilling & Cuzzi 1993).

More recently, it was found that the truth may lie in a combination of both models (Gammie 1996; Stepinski 1999; Ciesla 2007). The magnetohydrodynamic simulations showed that in a fully turbulent Kelvin–Helmholtz-driven disk, turbulence-free "dead zones" appear at places where dust prevents the ionization of gas. In this modern paradigm of protoplanetary dust

growth, fast migration of large dust aggregates as well as fast winds (above/below the sub-disk) occur at different regions in the nebula. If large dust aggregates and micrometer-sized particles coexist in the nebula, then all of the above scenarios lead to high-speed collisions between them. Thus, to understand planetesimal formation under the various scenarios described above, it is essential to understand the collision physics of the dust aggregates embedded in the protoplanetary disk. In a series of experimental papers, which are listed in Blum & Wurm (2008), the growth models of coagulation by Brownian motion and relative drift motions used in Weidenschilling & Cuzzi (1993) and Cuzzi et al. (1993) were basically confirmed and refined. A recent dust-growth model by Zsom et al. (2010), which is based upon an elaborate dust-aggregate collision model (Güttler et al. 2010), shows that the maximum dust-aggregate size in a minimum-mass solar nebula model is around 1 cm, due to the overwhelming effect of bouncing in aggregate–aggregate collisions.

Thus, realistic dust-growth models have two problems: (1) they fail to describe the formation of meter-sized (and larger) particles and (2) they fail to explain the large amount of micrometer-sized particles observed in protoplanetary disks without a dust-retention mechanism (Dullemond & Dominik 2005). While the latter is a real shortcoming of the models, the former might be an indication of the non-existence or short survival lifetimes of large protoplanetary dust aggregates. To overcome the depletion of small grains, Okuzumi (2009), Okuzumi et al. (2011a), and Okuzumi et al. (2011b) found that in case they are charged their coagulation is suppressed.

In this paper, we hypothesize that dust aggregates of considerable size (e.g., meter size) exist and we follow the evolution of these bodies in the protoplanetary disk. We will experimentally show that high-velocity impacts of micrometer-sized grains into large dust agglomerates are a strong source of further
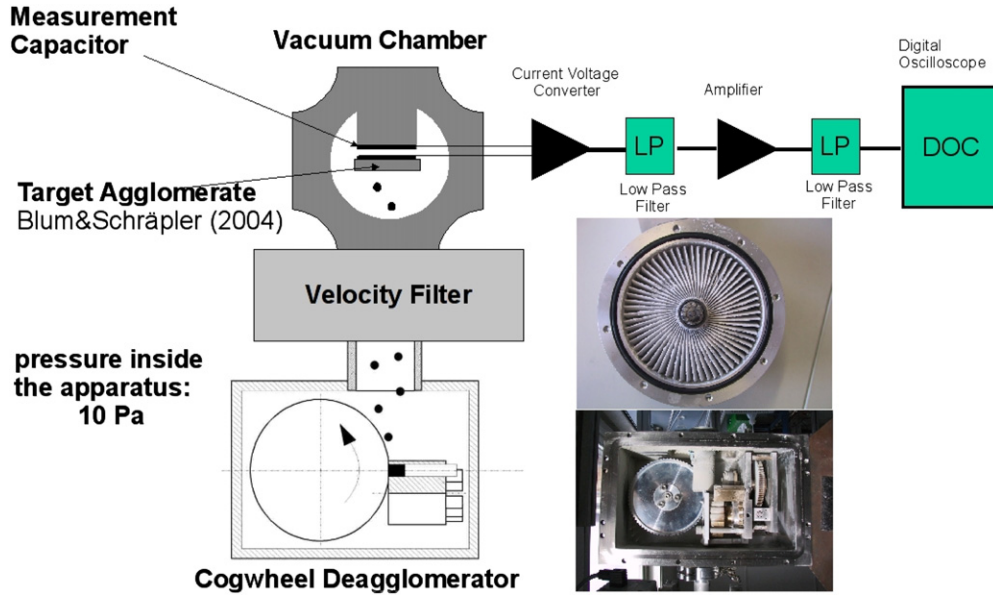
Figure 1. Schematics of the experimental setup, consisting of a vacuum chamber, which houses the target, the velocity filter (see upper inset photograph), the cogwheel (see lower inset photograph), the charge-measurement capacitor, and the measurement electronics.
(A color version of this figure is available in the online journal.)

micrometer-sized particles, which considerably limits the size of the largest surviving bodies.

The experimental method and the laboratory setup to perform collisions between micrometer-sized particles and dust aggregates are described in Section 2. In Section 3, the experimental results and their analyses are given, along with a numerical model that explains and confirms the experimental results. In Section 4, the experimental outcomes are applied to turbulent protoplanetary α-disks with values of the turbulence parameter $\alpha = 10^{-2}$ and $\alpha = 10^{-4}$, which shows the consequences of the erosional process on the population of micrometer-sized and decimeter-sized particles at different Kepler radii. In this section, we also compare our findings to recent infrared observations of protoplanetary disks by Furlan et al. (2006).

2. EXPERIMENTAL APPROACH

2.1. Mechanical Part

To reproduce the collision scenario following the paradigms described in Section 1, which preferentially leads to collisions between the smallest and the largest constituents of the dust size distribution, we developed a laboratory experiment in which collisions between micrometer-sized dust grains (projectiles) and centimeter-sized porous dust aggregates (targets; simulating the surfaces of much larger bodies) can be studied. As an analog dust material for the projectiles, we use spherical SiO_2 particles with a diameter of 1.5 μm (see Blum & Schräpler 2004). Thus, our projectile particles have sizes typical for protoplanetary dust, consist of a silicate-like material, and have a morphology suitable for theoretical modeling. The targets were produced by random ballistic deposition (RBD) out of the same particles and have a volume filling factor of $\phi = 0.15$ (see Blum & Schräpler 2004; Blum et al. 2006). RBD agglomerates have the same volume filling factor (and, thus, porosity) as the ballistic particle-cluster agglomerates which should dominate the dust-aggregate structures if aggregates preferentially grow by collection of small grains.

To simulate the projectile–target collisions hypothesized for the protoplanetary disk, a jet of fast projectiles is directed to centimeter-sized targets in a vacuum environment. The mass loss or gain of the targets is determined by precision weighing of the targets before and after exposure to a well-determined flux of projectiles. The experimental apparatus consists of a dust-dispersion cogwheel, a velocity filter, and a vacuum chamber, which contains the target (see Figure 1). The inside of the apparatus has a residual gas pressure of <4 Pa to prevent the particles from losing kinetic energy due to friction with the gas. The surfaces of the inside of the experiment are covered with vacuum grease on which the particles inevitably stick upon impact. Thus, only particles on ballistic trajectories from the cogwheel through the velocity filter can reach the target. To avoid ejected particles from falling back to the surface of the target agglomerate, the dust jet is directed in a vertically upward direction.

The particle jet is produced with a fast rotating cogwheel (see Figure 1), which also deagglomerates the powder dust sample into single monomer grains. The cogwheel is fed with dust from 20 dust reservoirs, which are arranged on a revolver. A piston presses the dust from a chosen reservoir against the fast rotating cogwheel. The deagglomerated particles possess up to twice the circumference velocity of the cogwheel, because they nearly elastically rebound from the cogs. The small amount of particles, which are not properly deagglomerated, impacts the cogwheel plastically and possesses velocities up to the circumference speed of the cogwheel. Due to this difference in velocity, it is possible to separate the non-deagglomerated particles from the monomer grains by a velocity filter. The velocity filter consists of an impeller with 60 blades (see Figure 1). The inclination of the blades is chosen such that their circumference covers 20° between the top and bottom of the impeller. If the impeller rotates at a constant speed, only particles within a preset velocity range can pass through the device. Particles that are either too fast or too slow hit the leading or the trailing blade of the impeller on which they stick, because the blades are covered with vacuum grease. We measured the velocity distribution of

the particles leaving the filter by illuminating the particles with a pulsed laser beam and observing their trajectories by a long-distance-microscope equipped with a high-speed camera. We found that the velocity of the particles leaving the velocity filter possess a full width at half-maximum (FWHM) of 17% of the optimum velocity given by the rotational speed of the filter. The velocity filter can be operated from 0 m s^{-1} to 90 m s^{-1}, but the cogwheel's deagglomeration efficiency drops dramatically at rotational speeds slower than 7.5 m s^{-1}. To calibrate the mass flow to the target, a greased target is placed inside the apparatus instead of the agglomerate target so that impacting particles will completely stick there. Thus, the mass arriving at the target area can be measured as a function of the dust mass provided to the cogwheel. In the second step of the measurement, the agglomerate target is weighed before and after the impact of a certain amount of particles. The strength of erosion (or growth) of the target can be determined by the ratio of the mass difference of the agglomerate before and after the exposure to the dust flux and the impacted mass. In a typical experiment, the target agglomerate is placed in the experimental chamber and the chamber is then evacuated. Upon reaching the desired vacuum, one to three dust cylinders are pressed against the rotating cogwheel. After each cylinder, the chamber is carefully vented to electrically discharge the target agglomerate. Then, the agglomerate is removed from the chamber and weighed. After weighing, the target is placed back inside the experimental chamber. In typical experiments, this procedure is repeated 2–10 times, depending on the experiment type.

2.2. Electrical Part

As known from previous experiments (Poppe & Schräpler 2005; Poppe et al. 2000a), particles in the dust jet produced by a cogwheel are heavily charged and possess a power-law charge–velocity distribution. To assess the influence of the particle charge on our erosion measurements, we measured the charge of the impactors and the charge transfer to the target agglomerate. This was done using the effect of electrical influence. The electrical setup is also shown in Figure 1. The target agglomerate is placed on one insulated plate of a measurement capacitor. If an electric charge is deposited on the target agglomerate, an identical charge is induced on the capacitor plate, which drives an electric current to the opposing capacitor plate. This current is amplified and logged by a digital oscilloscope, which is connected to a computer. The charge on the dust agglomerate is determined by integration of the electric current over time. To measure the charge of the projectiles and compare our measurement method with those of Poppe & Schräpler (2005), a greased target was placed on the measurement capacitor instead of the target agglomerate. All impacting particles stick on the greased target and keep their charge. The number of elementary charges on particles, accelerated to velocities of 15, 30, 45, and 60 m s^{-1}, was measured. A typical current profile during an experiment is shown in Figure 2.

By weighing the greased target before and after the impact of the particles, the charge per particle could be determined. The average numbers of elementary charges on each monomer particle accelerated to velocities of 15, 30, 45, and 60 m s^{-1} are 44, 198, 318, and 484 e^-, respectively, which are in good agreement with the measurements by Poppe & Schräpler (2005) and Poppe et al. (2000a). As a result of the charged dust target, the impactors lose kinetic energy before an impact. The calculation of the energy loss due to the electric potential was
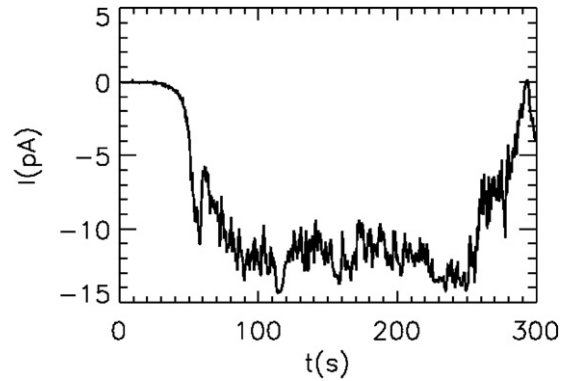
Figure 2. Typical electric current profile when a greased target is exposed to a dust jet with 15 m s^{-1} impact velocity. The dust flow starts at $t \approx 50$ s and ends at $t \approx 300$ s. The dust jet is generated by pressing one dust cylinder against the cogwheel.

approximated by assuming the target agglomerate as a charged sphere with the radius of the target diameter and the charged particles as test charges arriving from infinity. These calculations were confirmed by a numerical simulation of the incoming particles using the exact geometry of the experimental setup with the software package COMSOL. In all measured parameters, the velocity loss of the impinging projectiles was smaller than 2%. The collision dynamics of the erosion process is not changed, because the required pull-off force of the particles is four orders of magnitude larger than the electric force close to the target surface. Charging of the particles and targets is therefore negligible for the following measurements.

Figure 3 shows an example of the influence of the projectile and target charging on the impact energy and velocity. In the top-left graph of Figure 3, the electric current to the target agglomerate caused by the impinging projectiles with a mass of 3.5×10^{-15} kg is shown. The current drops to zero after a certain number of particles have impacted. This is due to the fact that particles are deposited to the surface and charges that are separated as a cause of the impact are also sitting on the surface. Each impact erodes particles from the agglomerate surface (see below) so that after a certain number of impacts, an equilibrium between deposited and separated charges (sitting on eroded particles) is reached. In the top-right graph of Figure 3, the total charge of the target agglomerate is given as a function of the accumulated mass flux of the impinging projectiles. Note that this charge is limited by the equilibrium discussed before. In the lower left graph of Figure 3, the total energy loss caused by Coulomb repulsion of an impinging particle is shown. In the lower right graph of Figure 3, the velocity loss of an impinging projectile is given, which is negligible compared to the initial velocity of 60 m s^{-1}.

3. EXPERIMENTAL RESULTS

3.1. Erosion and Passivation

We performed the impact experiments described in Section 2 at impact velocities of 15, 30, 44, and 59 m s^{-1}, respectively. A surprising result is that the erosion efficiency (i.e., the relative mass loss of the target) depends on the impact history of the (initially highly porous) target agglomerate, as can be seen in Figure 4 for impacts with 59 m s^{-1} projectile velocity. The data points show the mass loss of the target agglomerate, Δm, per impinging monomer mass, $m_i = 3.5 \times 10^{-15}$ kg, as a function of the total-mass exposure per unit cross section onto the target, μ. One can see from the saturation of the curve that the target
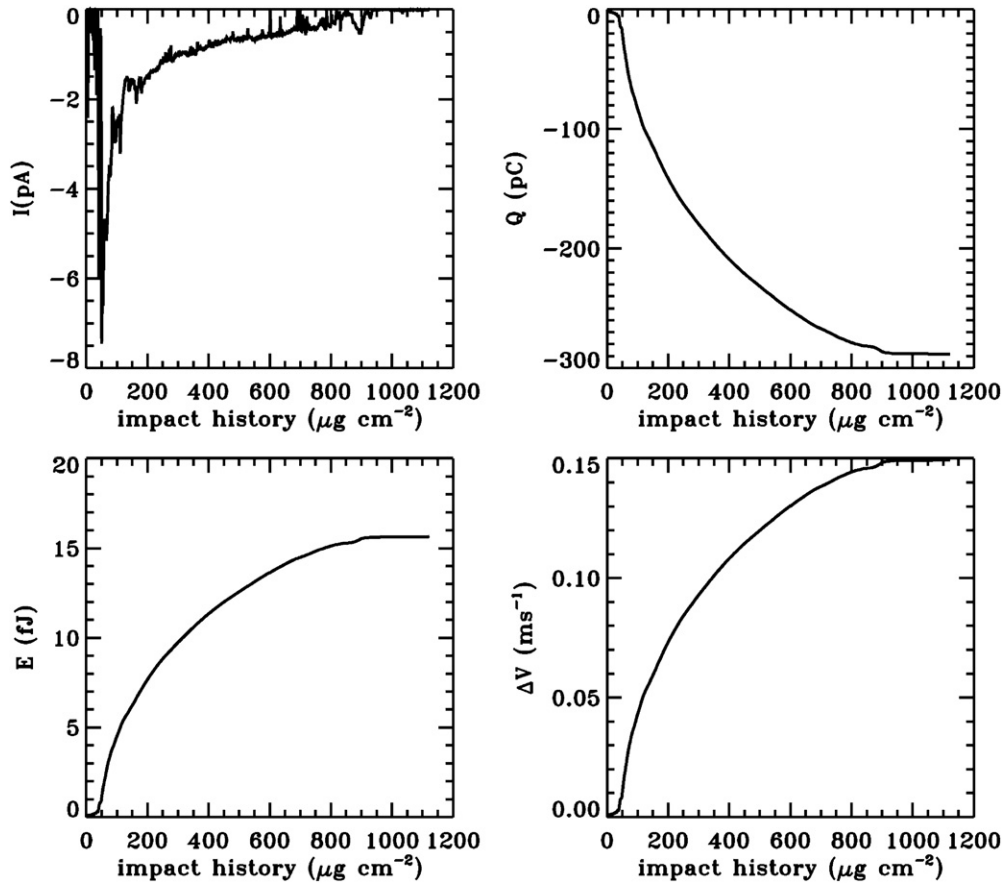
Figure 3. Examples of the influence of electric charges on the collision behavior of micrometer-sized dust projectiles (with a mass of 3.5×10^{-15} kg) impacting a porous dust-aggregate target at 60 m s^{-1} velocity. Top left: the profile of the electric current over the total amount of dust exposure. Top right: the total charge accumulated by the target. Lower left: the calculated energy loss of a charged projectile carrying 1000 elementary charges. Lower right: the calculated velocity loss of a charged projectile carrying 1000 elementary charges with an initial velocity of 60 m s^{-1}.
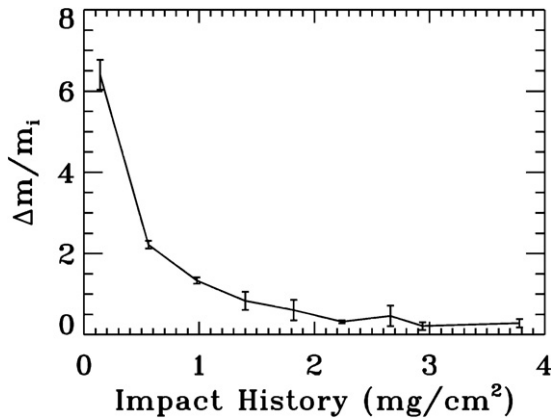
Figure 4. Erosion efficiency of monomer projectiles impinging a target agglomerate at 59 m s^{-1}. The saturation of the erosion efficiency for $\mu \gtrsim$ 2 mg cm^{-2} is clearly visible. The error bars result from the measurement uncertainty of the weighing process.
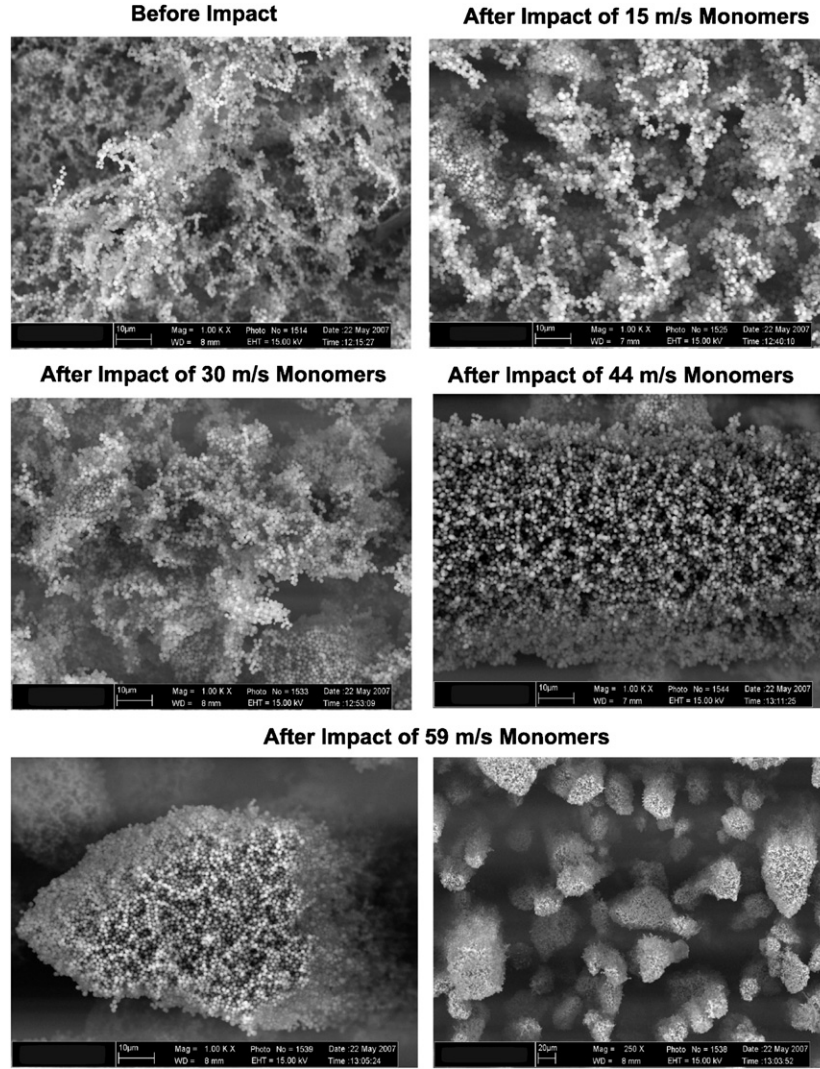
agglomerate is passivated against erosion for mass exposures $\mu \gtrsim 2$ mg cm^{-2}. This saturation mass exposure is about 20 times the number of particles on the surface layer of an unprocessed agglomerate. Experiments with impact velocities of 15, 30, 44, and 59 m s^{-1} show a similar saturation behavior. The error bars in Figure 4 denote the measurement uncertainties of the weighing process. The erosion efficiency at the initial and final stage for all measured impact velocities is shown in Figure 5. The velocity error bars denote the velocity dispersion due to
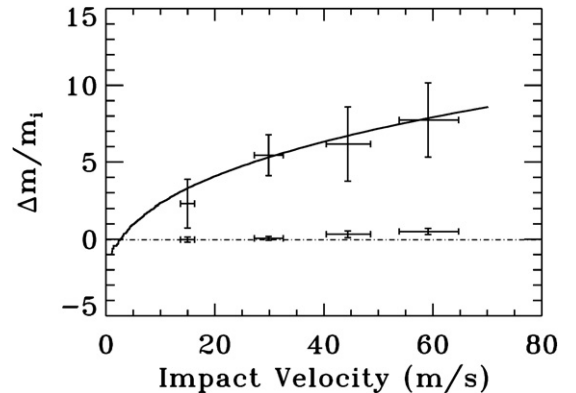
Figure 5. Erosion efficiency of target agglomerates for impact velocities of 15, 30, 44, and 59 m s^{-1}, respectively. The upper data points with error bars were recorded at the onset of the experiment, in which the target agglomerate was very porous and not yet passivated, whereas the lower data points with error bars show a reduced erosion efficiency after the target-agglomerate's surface was almost passivated against erosion. The velocity error bars denote the velocity distribution stemming from the velocity filter. The vertical error bars denote one standard deviation of several measurements with different target agglomerates. The solid curve follows Equation (8) and is the result of a numerical impact model described in Section 3.2.2.

the width of the velocity filter. The error bars in the vertical direction are the standard deviation of several measurements with different target agglomerates. Figure 5 shows that the initial erosion efficiency scales with impact velocity but is reduced to a saturation level of zero for impact velocities lower than 26 m s^{-1}.

Before Impact   **After Impact of 15 m/s Monomers**

After Impact of 30 m/s Monomers   **After Impact of 44 m/s Monomers**

After Impact of 59 m/s Monomers

Figure 6. SEM images of the surface of a target agglomerates before and after the passivation by dust-particle impacts at velocities of 15, 30, 44, and 59 m s^{-1}, respectively. The scale bars at the bottom left of each SEM image are 20 μm for the bottom-right image and 10 μm for the other images.

For higher impact velocities, the erosion efficiency is reduced to about 15% of its initial value. The reduction of the erosive effect of the particle impacts goes along with a compaction of the surface. Figure 6 shows scanning electron microscopy (SEM) images of the target agglomerate's surface before and after an exposure to dust fluxes at 15, 30, 44, and 59 m s^{-1}, respectively. An obvious change in surface structure occurs between 30 and 44 m s^{-1}.

3.2. Theoretical Considerations

3.2.1. Analytical Part

A key to understanding the erosion behavior described above is given in the work of Konstandopoulos (2000). He numerically simulated the formation of agglomerates by the RBD process and discovered that the coordination number n (i.e., the number of next neighbors) in an agglomerate increases with increasing impact velocity of the depositing particles, until a maximum coordination number of $n_{max} = 6$ is reached. Note that the maximum coordination number found by Konstandopoulos (2000) has a Gaussian distribution with an FWHM of 2. Konstandopoulos (2000) found that a relation fits his numerical results which reduces the collision of a single particle with a particle bound in a large agglomerate to a collision of a single particle with another single particle of an effective mass given by

$$m_{eff} = m(1 + Cn), \quad (1)$$

where C is a dimensionless deposit "rigidity" parameter in the range $(1, \infty)$, m is the mass of the particle bound to the agglomerate, and n its local coordination number. Using Equation (1) and applying momentum and energy equations, we calculated the energy transferred to an effective particle to

$$E_{eff} = 4E_{imp} \frac{1 + Cn}{(2 + Cn)^2}, \quad (2)$$

with E_{imp} denoting the kinetic energy of the impactor. The energy to release a particle from an agglomerate is given by

$$E_r = E_c n, \quad (3)$$

where E_c is the breakup energy of a single particle–particle contact. An empirical relation for the capture threshold velocity v_{st} can be deduced from the experiments by Poppe et al. (2000b), who showed that

$$v_{st} = 0.92 \left(\frac{a_0}{\mu m} \right)^{-0.52} \text{m s}^{-1}, \quad (4)$$
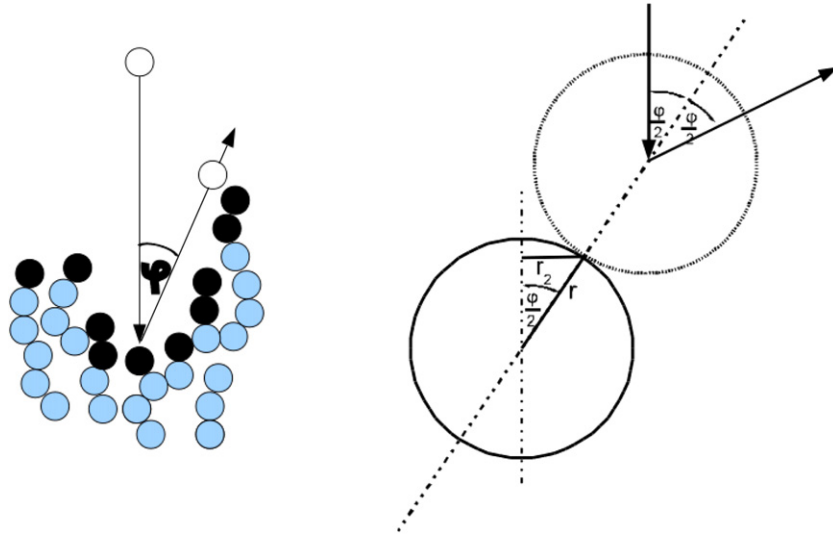
Figure 7. Left picture: an impacting particle (white) is shown that is reflected off an agglomerates surface at an angle φ. The black particles are surface particles that can be reached by the impinging particle. The gray particles are bulk particles of the agglomerate that cannot be reached. The angle φ corresponds to the probability that the impactor can impact a second time. Right picture: relation between the maximum escape angle and the probability of a second impact of the impinging particle $r_2 r^{-1}$.

(A color version of this figure is available in the online journal.)

with a_0 being the monomer radius. Based on this relation, we can derive the breakup energy of a particle contact to be

$$E_c = \left(\frac{1}{2}\right)^{\frac{7}{3}} m_0 v_{st}^2 \qquad (5)$$

(Blum & Wurm 2000) with m_0 being the mass of the impacting monomer. It is obvious from Figure 6 that the target agglomerate gets compacted by the impinging dust projectiles. An increased compression, i.e., an increased volume filling factor ϕ results in an increased coordination number (van de Lagemaat et al. 2001). The increased coordination number increases the release energy of a particle and is a mechanism that passivates the agglomerate.

3.2.2. Numerical Description of an Unpassivated Target Agglomerate

Dominik & Tielens (1997) and Wada et al. (2008) predict an erosion effect proportional to the impact energy, thus proportional to the squared impact velocity, which is in contradiction to our experimental results (see Figure 5). To validate our measurements by theory, we developed a numerical model that applies the collision model of Chokshi et al. (1993) with the adaptation recommended by Blum & Wurm (2000). In our model, the energy loss of a repelling particle equals its binding energy and the effective mass term (Equation (1)) of Konstandopoulos (2000) is used. The effective mass term requires a rigidity parameter C. For fluffy agglomerates, Konstandopoulos (2000) chose it close to 1 to get realistic results. Therefore, we also chose a value 1 for the rigidity parameter. In our model, all particles of an agglomerate have an effective mass corresponding to their coordination number and thus only part of the impactor's kinetic energy is transferred to the respective agglomerate monomer. The remaining kinetic energy of the impactor after its impact is either used in a further impact or is lost if the particle escapes from the agglomerate. The escape probability Ξ of the impactor and the ejected particles is calculated from the surface texture of a numerically grown RBD agglomerate (see Blum et al. 2006). This calculation is done in three steps. In the first step, all particles that can be reached by impinging particles from a direction perpendicular to the (mean) target surface are identified and

defined as surface particles (see Figure 7). Depending on the fraction of the particles on the aggregate's surface that can be reached by impinging particles of the same size, a corresponding accessibility is calculated. In a second step, the angles of the surface particles are calculated under which they can escape without impacting again with the target agglomerate after they are released by the original projectile. The same is done for the reflected impactor. For simplicity, this procedure is not applied to all particles and neighbor particles on the agglomerate surface. The problem was reduced to a two-dimensional problem.

Only particles on a given line on the surface are taken into account, and to calculate the required angles, only particles are used that are found in one direction of that line. It is therefore assumed that the target surface is isotropic. The smallest of the angles from a given particle on the line to its neighbors in one direction is the maximum escape angle (see Figure 7). By repeating this procedure for a large number of particles on the defined line on the agglomerate's surface and by averaging over the occurring angles, the mean escape angle is determined.

The probability to impact a further particle is calculated by assuming that this is the case if the reflection angle is larger than the mean escape angle. The probability of a particle to fulfill this condition is found by taking into account that all particles are spherical. The reflection angle of a particle impinging perpendicular to the agglomerates surface is connected with the impact distance from the target particle's axis r_2 in the agglomerate (see Figure 7).

The correspondence between the reflection angle and the probability of an reflection angle larger than ϕ is given by

$$\Xi = \frac{r - r_2}{r} \qquad (6)$$

which corresponds to

$$\Xi = 1 - \sin\frac{\phi}{2} \qquad (7)$$

(see Figure 7). These probabilities are multiplied with the corresponding accessibility of that given particle and averaged over

all considered particles. We found that for RBD agglomerates $\Xi = 0.39$.

If the energy transferred to the agglomerate target exceeds the binding energy of the monomer grain, it will be ejected and will impact another agglomerate monomer with a probability of $1 - \Xi$. This corresponds to the fact that the mean coordination number of the (initial) target agglomerate is 2, which means that it is an agglomerate of particle chains. It is very unlikely for an impactor to hit the end of a chain in a direction parallel to the chain. In all the other impacts, the hit particle can be directly ejected. This is not the case for a compacted agglomerate with a larger mean coordination number.

The contact energy E_c of a monomer particles required for the modified Chokshi et al. (1993) model (see also Dominik & Tielens 1997) is taken from Poppe et al. (2000b). The coordination number distribution of the particles at the agglomerate's surface and the surface texture of the agglomerate are also calculated from the numerically grown RBD agglomerate (Blum et al. 2006). Our numerical erosion model is realized as a statistical code with recursive elements. This means that all possible impacts (concerning the effective mass of the target particles) of an impinging particle are calculated, multiplied with the probability to release a particle and summed up. All possible impacts of the reflected impactor and the ejected particles are multiplied with the probability of a further impact and the probability of the occurrence of the effective masses of the targets and are also summed if their impact energy is large enough to release a particle. This is done in a recursive way until the particle energy of a given branch of the simulation is lower than E_c which then leads to sticking. In other words, to get the total number of particles that are ejected by the impact of a given particle, the probabilities of all possibilities to eject a particle are summed up, where the possibility to eject a certain particle is the product of all possibilities of the preceding path of the impactor. The outcome of the impact simulation on the unprocessed agglomerate is shown as a solid curve in Figure 5. It can be fitted for impact velocities larger than 15 m s^{-1} by a square root function

$$\frac{\Delta m}{m_i} = \sqrt{\frac{1.25 v_{\text{imp}}}{1 \, \text{m s}^{-1}} - 7.5}. \qquad (8)$$

In the region lower than 15 m s^{-1} sticking can occur, which considerably reduces the erosion efficiency. For velocities below 2.7 m s^{-1}, sticking dominates the impact process, which leads to a net growth of the agglomerate, i.e., $\Delta m/m_i < 0$. At velocities lower than 1 m s^{-1} all impactors stick, i.e., $\Delta m/m_i = -1$.

3.2.3. Numerical Description of a Passivated Target Agglomerate

In a passivated agglomerate, the projectiles impact perpendicular to the surface of interconnected particles. The ejection of such a particle requires more energy than for the loosely bound monomers in the RBD targets. As no numerical agglomerate for passivated targets is available, we have to rely on the structural information provided by the SEM pictures, which are two-dimensional. Therefore, it is not possible to exactly measure the coordination number of a passivated agglomerate. We also choose $C = 1$ for this simulation. The coordination number of 6 found by Konstandopoulos (2000) leads to a too perfect passivation at nearly all velocities. K. Wada (2009, private communication) found in molecular-dynamics calculations that agglomerates that are processed by collisions tend toward a mean coordination number of 4. Therefore, we chose a mean coordination number distribution on the agglomerate surface of
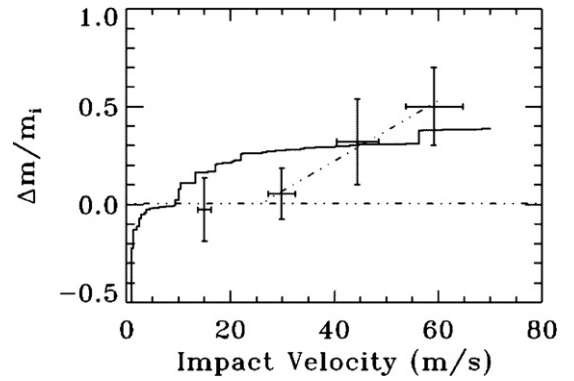
Figure 8. Erosion efficiency as a function of impact velocity for a passivated agglomerate target. The crosses denote the experimental values with error bars; the solid line shows the result of our numerical model. The double-dot-dashed lines mark the zero erosion line and the fit for the velocity-dependent erosion given in Equation (9) and used in Section 4.

3 with a Gaussian distribution of an FWHM of 2. The passivated agglomerates show a steep valley-hill structure (see Figure 6, bottom right).

SEM images of the type shown in Figure 6 were used to estimate the probability Ξ_p that an ejected or reflected particle will again impact at the agglomerate. In a passivated agglomerate, the monomers bound in the agglomerate cannot be directly ejected as it was the case with the unpassivated agglomerates, which mainly consists of particle chains. After an impactor hits a monomer bound in a passivated agglomerate, the bound monomer itself impacts its up to five neighbors. If its kinetic energy after this multiple impact is higher than the binding energy to its neighbors, the monomer is ejected. In our numerical code, all possible impacts with respect to the coordination number distribution were calculated and multiplied with the estimated occurrence of each coordination number. Any target monomer that is hit by any other monomer particle (projectile or ejected target monomer) can again impact its neighbor particles in a recursive way. All ejected particles can again impact on the agglomerate with the probability of Ξ_p. Please note that because of the lacking information on the internal structure of the passivated agglomerate, this numerical method can only be a rough estimate. As a result of our crude model for passivated targets (see Figure 8), it was found that the order of magnitude of the agglomerate passivation against erosion can be reproduced by the numerical model. However, due to the crude assumptions of our model, it is not able to reproduce the detailed characteristics of the erosion efficiency as a function of impact velocity. Thus, for the following application (Section 4), the measured values are used via a linear interpolation function of the measured data

$$\frac{\Delta m}{m_i} = a v_{\text{imp}} + b \qquad (9)$$

with $a = 0.0155 \, \text{s m}^{-1}$ and $b = -0.4$ in the velocity range $26 \, \text{m s}^{-1} \leqslant v \leqslant 60 \, \text{m s}^{-1}$.

4. APPLICATION TO A PROTOPLANETARY DISK

4.1. Grain Population in a Solar Nebula

To estimate the influence of the erosion process on the dust-aggregate distribution in a protoplanetary nebula, a simple analytical model based on the timescales of the erosion and

coagulation processes will be developed and compared to observational findings in the following section. For this, we use a standard minimum-mass protoplanetary nebula with a disk mass of 0.0425 $M_\odot$. The analytical disk model is taken from Schräpler & Henning (2004, their Appendix A1). This leads to a surface mass density at 1 AU of 1.7×10^4 kg m^{-2} and a gas density in the midplane at 1 AU of 1.4×10^{-6} kg m^{-3} and 280 K at 1 AU. The dust mass is 1% of the gas mass. The relative velocities of the particles are taken from Weidenschilling (1977, his Figures 3 and 5) and approximated and extrapolated in Equations (11), (55), and (56). The number of large particles n_m is calculated for a given Kepler radius by assuming that 70% of the total mass is in the large dust agglomerates with a size given in Figures 10 and 11 (bottom graph, solid line). The total-mass ratio of 70% for the large dust aggregates is taken from Nomura & Nakagawa (2006, their Figure 5) after one coagulation timescale, the radii of the large dust aggregates are taken from Nomura & Nakagawa (2006, their Figure 6, dash-dotted line). An increase of the total mass in the large agglomerates to 90% of the total mass, which would be the case after two coagulation timescales in Nomura & Nakagawa (2006, their Figure 5) leads to minor changes of our results that would be hardly visible in Figures 10 and 11. We ignored icy grains at outer disk radii. The threshold impact velocity for erosion should be considerably higher for icy particles. However, the predominant part of the erosion takes place at Kepler radii below 2 AU.

4.1.1. The Erosive Formation of Monomer Dust Grains and Their Subsequent Coagulation

Most of the coagulation models (e.g., Nomura & Nakagawa 2006) show that micrometer-sized particles vanish from the nebula on a very short timescale, due to their effective coagulation. Therefore, it is important to calculate whether the source of small dust grains released by the erosion of large dust aggregates, as described in the previous sections, is strong enough to compensate the loss of the dust particles by coagulation. As we have shown above, a small initial number of micrometer-sized dust grains is sufficient to start the erosion process of aggregates with sizes of decimeter and above. The particle production rate in a differential volume element $dV = 2\pi R H dr$ (see Figure 9) is given by

$$\frac{d(dN)}{dt} = \rho_0 \, n \, v_{\rm imp} \, f \, dA_m, \qquad (10)$$

where the relative velocity between the micrometer-sized particles and the large agglomerates is taken from Weidenschilling (1977) and approximated for Kepler radii larger than 0.2 AU to

$$v_{\rm imp} = 50({\rm m\ s}^{-1}) R({\rm AU})^{-\frac{1}{3}}. \qquad (11)$$

Here, $f(v_{\rm imp})$ is the number of monomer grains ejected by an impacting particle, ρ_0 is the number density of micrometer-sized particles in the midplane of a protoplanetary disk, and n is the number of large dust aggregates at a disk area $A_D = 2\pi R r$, where it is implicitly assumed that most of these large aggregates are located close to the midplane. This area element is chosen because all particles located in there cut the differential volume element dV with their front side in the velocity direction. Therefore, the number n can be expressed by the surface density δ of large agglomerates

$$n = \delta 2\pi R r. \qquad (12)$$
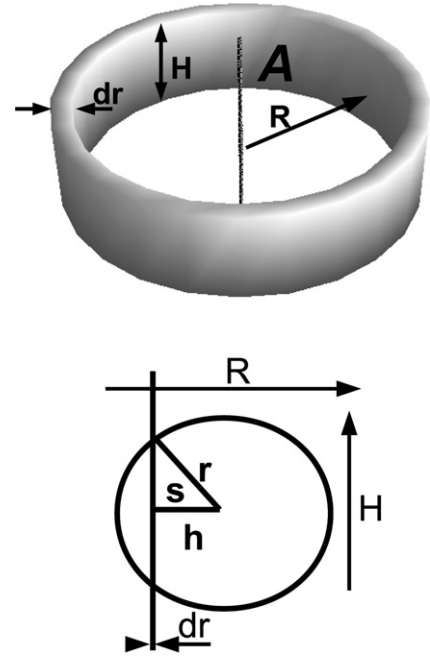
Figure 9. Upper picture: the differential volume element dV, which is a torus in the protoplanetary nebula at the orbital distance R with a height H and a thickness of dr. Lower picture: a large particle with a radius r at a radial distance s from dV in the midplane of the disk. As $s \leqslant r$ an area of intersection forms as a ring with a radius s and a thickness dr.

The mean differential area with which the particles inside A_D cut dV, is given by

$$dA_m = 2\pi \frac{dr}{r} \int_r^0 s \, ds. \qquad (13)$$

With

$$s = \sqrt{r^2 - h^2} \text{ and } ds = -\frac{h\,dh}{\sqrt{r^2 - h^2}} \qquad (14)$$

we obtain

$$dA_m = \pi r \, dr, \qquad (15)$$

assuming that all particles are homogeneously distributed in A_D. Here, h is the distance of the center of a given particle to dV (see Figure 9).

The number of micrometer-sized particles produced within a given radius element $2\pi R dr$ is dN, which will in the following be expressed using the corresponding particle number density in the midplane ρ_0. The differential surface density of the particle number dN at a given radius element $2\pi R dr$ is

$$\Sigma = \frac{dN}{2\pi R dr}. \qquad (16)$$

The integration

$$\Sigma = \int_{-\infty}^{\infty} \rho(z) dz \qquad (17)$$

of the vertical number density structure

$$\rho(z) = \rho_0 \exp\left(-\frac{z^2}{2H^2}\right) \qquad (18)$$

in the protoplanetary nebula results in

$$\rho_0 = \frac{\Sigma}{H\sqrt{2\pi}}. \qquad (19)$$

Inserting Equation (16) yields

$$dN = \rho_0 (2\pi)^{\frac{3}{2}} RH dr \qquad (20)$$

and

$$\frac{d(dN)}{dt} = \frac{d\rho_0}{dt}(2\pi)^{\frac{3}{2}} RH dr. \qquad (21)$$

Inserting Equations (21), (12), and (15) into Equation (10) results in

$$\frac{d\rho_0}{dt} = \rho_0 \frac{r^2 \delta v_{\text{imp}} f \sqrt{\pi}}{\sqrt{2}H}, \qquad (22)$$

which is the differential equation for the dust number density increase of micrometer-sized particles without coagulation.

In the following step, we will introduce the coagulation of the micrometer-sized particles. For simplicity and as a lower limit to the erosion efficiency, we assume that all micrometer-sized particles that coagulate to dimers or larger aggregates are lost to the erosion process. This assumption leads to the equation

$$\frac{d\rho}{dt} = -\sigma v_B \rho^2 \qquad (23)$$

(Blum 2004), where we assumed that the main source of the inter-particle collisions is the Brownian motion with a mean collision velocity v_B and σ is the cross section in the collision of two micrometer-sized particles and ρ is given by Equation (18). Because micrometer-sized particles are perfectly coupled to the disk gas, turbulence effects are negligible. To calculate the coagulation particle losses, we have to take into account that the coagulation efficiency depends on ρ and therefore on the disk scale height H. Because dust particles of μm size are mixed over H on a timescale of an orbital period it is possible to integrate both sides of Equation (23) over the disk height following Brauer et al. (2008, in their Appendix B) which results in

$$\frac{d\Sigma}{dt} = -\sqrt{\pi} H \sigma v_B \rho_0^2. \qquad (24)$$

With Equation (19) we obtain an equation for the midplane number density of monomers

$$\frac{d\rho_0}{dt} = -\frac{\sigma v_B \rho_0^2}{\sqrt{2}}. \qquad (25)$$

Performing the coagulation feedback by adding Equation (25) to the right-hand side of Equation (22) results in

$$\frac{d\rho_0}{dt} = \Theta \rho_0 - \Phi \rho_0^2 \qquad (26)$$

with

$$\Theta = \frac{r^2 \delta v_{\text{imp}} f \sqrt{\pi}}{\sqrt{2}H}, \qquad (27)$$

$$\Phi = \frac{\sigma v_B}{\sqrt{2}}, \qquad (28)$$

whose solution is

$$\rho_0(t) = \rho_{00} \frac{\Theta \exp(\Theta t)}{\Theta + \rho_{00}\Phi(\exp \Theta t - 1)}. \qquad (29)$$

Here, ρ_{00} is the initial number density of micrometer-sized dust. The half-value time of the above equation,

$$t_2 = \frac{1}{\Theta} \ln \left(\frac{\rho_{00}\Phi - \Theta}{\rho_{00}\Phi - 0.5\Theta} \right), \qquad (30)$$

seems to be dependent on ρ_{00}, but for a typical protoplanetary nebula $\Theta \gg \rho_{00}\Phi$, which is valid for any reasonable ρ_{00}. Therefore, the half-value time is

$$t_2 \approx \frac{1}{\Theta} \ln 2. \qquad (31)$$

For a minimum-mass solar nebula at 1 AU t_2 is about two years. Because H is roughly proportional to R, t_2 approximately scales with the Kepler radius squared. As we will see later, it is of the same order as the timescale for erosional radius loss of large particles. Therefore, the stationary solution of Equation (26) is used in the following as a zero-order approximation, i.e.,

$$\rho_{0s} = \frac{r^2 \delta v_{\text{imp}} f \sqrt{\pi}}{H \sigma v_B}. \qquad (32)$$

4.1.2. Timescale of the Erosive Radius Loss of Large Dust Aggregates

The number of the monomers eroded from a large dust aggregate per unit time is given by

$$\frac{de}{dt} = -r^2 \pi v_{\text{imp}} f \rho_{0s}. \qquad (33)$$

The relation between the radius of a large particle r and the number of monomer grains e inside the aggregate is

$$e = \frac{\frac{4}{3}r^3 \pi l}{V_\mu}. \qquad (34)$$

Here, l is the filling factor of the large dust aggregate and V_μ denotes the volume of a micrometer-sized particle. Differentiation by t gives

$$\frac{de}{dt} = \frac{4r^2 \pi l}{V_\mu} \frac{dr}{dt}. \qquad (35)$$

Combining Equations (33) and (35) results in

$$\frac{dr}{dt} = -\frac{1}{4l} v_{\text{imp}} f \rho_{0s} V_\mu. \qquad (36)$$

The value v_{imp} does not depend on r for particle sizes larger than 0.3 m in Weidenschilling (1977, his Figure 2). Due to an expected filling factor of 0.4 for macroscopic protoplanetary dust aggregates and a bulk density of 2000 kg m^{-3} (see Zsom et al. 2010), which leads to an aggregate density of 800 kg m^{-3}, we re-calculated the relative velocities of Weidenschilling (1977) for aggregates of 40% filling factor. For these dust aggregates, the velocity does not depend on the aggregate size for radii larger than 0.6 m at 1AU, which is in the zeroth-order approximation also the case for larger Kepler radii with $r_0 = 1$ m. Inserting Equation (32) into Equation (36) gives

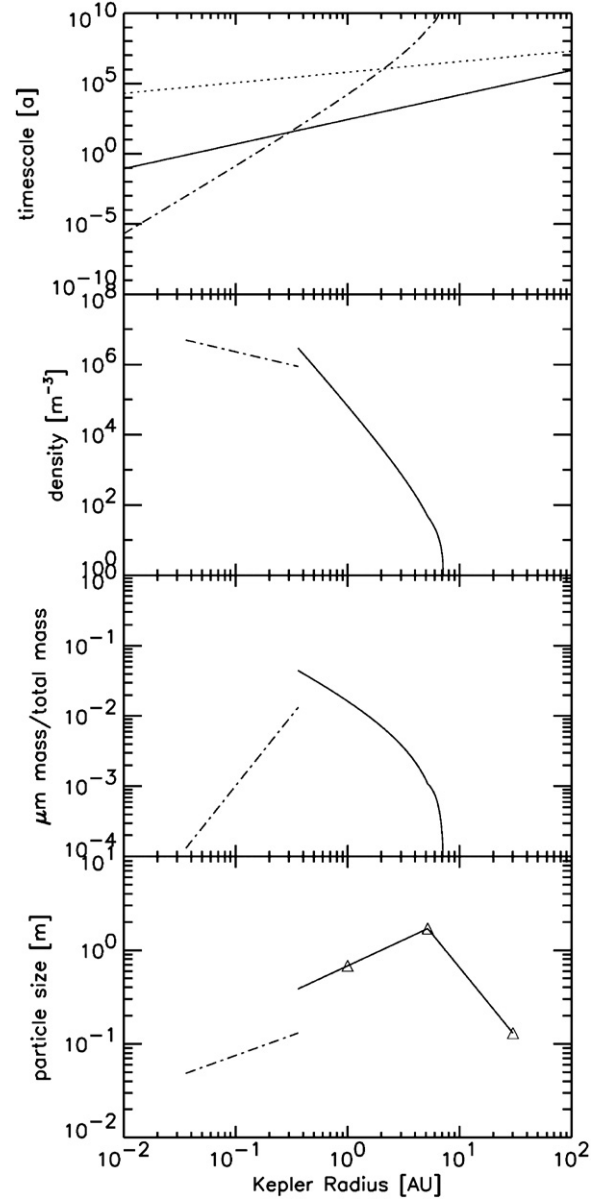$$\frac{dr}{dt} = -\frac{v_{\text{imp}}^2 f^2 V_\mu \delta r^2 \sqrt{\pi}}{4l H \sigma v_B} \qquad (37)$$
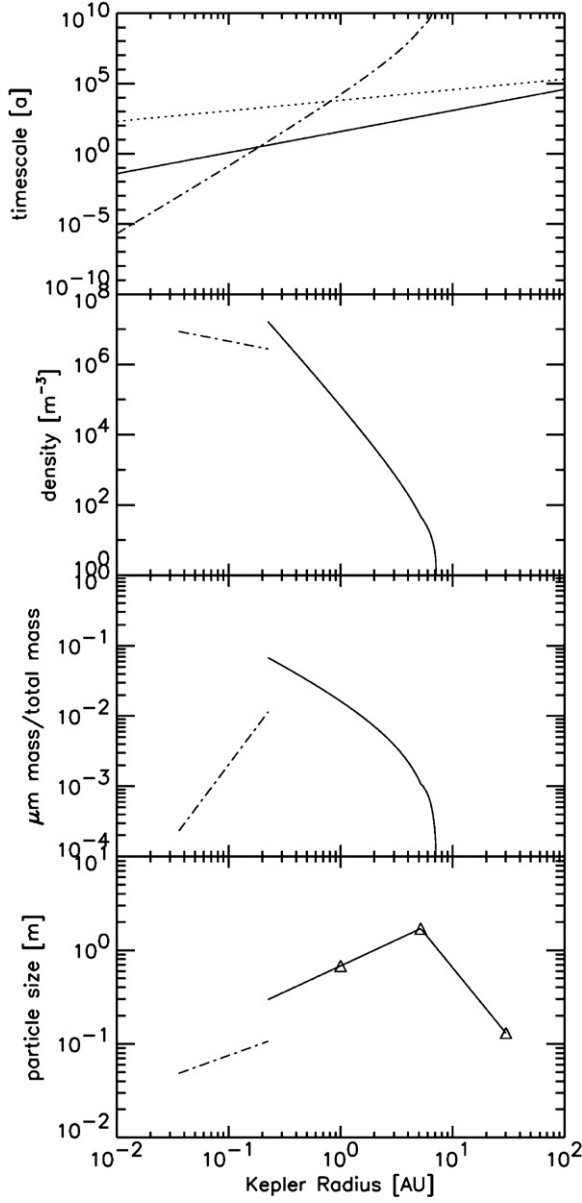
Figure 10. Protoplanetary disk with $\alpha = 10^{-2}$. Top graph: coagulation timescale (solid line), erosional timescale (dash-dotted line), radial turbulent transport (dotted line). Second graph: number density of micrometer-sized particles at erosion timescale larger than the coagulation timescale (solid line), number density of micrometer-sized particles at erosion timescale smaller than the coagulation timescale (dash-dotted line). Third graph: ratio of the total mass of micrometer-sized particles to the total dust mass at a given Kepler radius. Bottom graph: particle size in which 70% of the total solid disk mass is contained (also maximum particle size) for erosion timescales larger than the coagulation timescale taken from Nomura & Nakagawa (2006; triangles) and their power-law interpolation (solid line). Maximum particle size for erosion timescales smaller than the coagulation timescale (dash-dotted line).

Figure 11. Protoplanetary disk with $\alpha = 10^{-4}$. Top graph: coagulation timescale (solid line), erosional timescale (dash-dotted line), radial turbulent transport (dotted line). Second graph: number density of micrometer-sized particles at erosion timescale larger than the coagulation timescale (solid line), number density of micrometer-sized particles at erosion timescale smaller than the coagulation timescale (dash-dotted line). Third graph: ratio of the total mass of micrometer-sized particles to the total dust mass at a given Kepler radius. Bottom graph: particle size in which 70% of the total solid disk mass is contained (also maximum particle size) for erosion timescales larger than the coagulation timescale taken from Nomura & Nakagawa (2006; triangles) and their power-law interpolation (solid line). Maximum particle size for erosion timescales smaller than the coagulation timescale (dash-dotted line).

whose solution is

$$r = \left(\frac{1}{r_0} + \frac{v_{\text{imp}}^2 f^2 V_\mu \delta \sqrt{\pi}}{4 l H \sigma v_B} t \right)^{-1}. \tag{38}$$

The corresponding half-value time of r is

$$t_{\frac{1}{2}} = \frac{4 l H \sigma v_B}{v_{\text{imp}}^2 f^2 V_\mu \delta r_0 \sqrt{\pi}}. \tag{39}$$

The erosion timescale as a function of the Kepler radius is given in Figures 10 and 11 (top graphs, dash-dotted lines) for turbulence parameters $\alpha = 10^{-2}$ and $\alpha = 10^{-4}$, respectively. The values for f for different velocities were taken from the data points of Figure 8, where it was assumed that the curves in between the data points are straight lines.

4.1.3. Passivation Timescale

To decide whether the erosion efficiencies of the unpassivated or the passivated agglomerates should be used to describe

the erosion processes in the solar nebula (see Figure 5), the passivation timescale needs to be estimated. The number of particles on the surface of an agglomerate is given by

$$N_{\text{surf}} = \frac{2\pi r^2 l^{\frac{2}{3}}}{2\pi r_{\mu\text{m}}^2}, \quad (40)$$

where $r_{\mu\text{m}}$ is the radius of a monomer. The rate at which monomer particles impact on a dust aggregate's surface is given by

$$\frac{dN_{\text{coll}}}{dt} = \rho_0 r^2 \pi v_{\text{imp}} f. \quad (41)$$

We found in Section 3.1 (e.g., Figure 4) that an agglomerate is passivated after about 10 times the number of surface monomers have impacted on the agglomerated. Thus, the passivation time is

$$t_{\text{pass}} = 10 N_{\text{surf}} / \frac{dN_{\text{coll}}}{dt}. \quad (42)$$

This passivation timescale t_{pass} is smaller than a day for all reasonable parameters and orbital radii in the disk. Therefore, passivated agglomerates are dominating the erosion process so that we use the experimental erosion efficiency from the passivated dust samples (double-dot-dashed line in Figure 8 and Equation (9)).

4.1.4. Coagulation Timescale

For the coagulation timescales, we use the results obtained by Nomura & Nakagawa (2006). Their model is based on the assumption that compact particles (with a filling factor of 100%) that grow to a certain size are removed from the coagulation process by radial drift. In other models (e.g., Blum 2004; Brauer et al. 2008; Zsom et al. 2010), the coagulation is counteracted by fragmentation and bouncing of colliding particles, which is not considered here. As macroscopic protoplanetary dust aggregates possess filling factors of about 40%, we will adapt the model by Nomura & Nakagawa (2006) to our non-compact dust aggregates. The coagulation timescale of Nomura & Nakagawa (2006) is given by

$$\tau_k = \frac{1}{\rho_{mi} A_{mi} v_r}, \quad (43)$$

with ρ_m, A_m, and v_r being the number density of dust aggregates with mass m, their collision cross sections, and the relative velocities, respectively.

The coagulation timescale τ_k depends on the filling factor l via the cross section

$$A_m = A_{m1} l^{-\frac{2}{3}}, \quad (44)$$

which leads to

$$\tau_k = l^{\frac{2}{3}} \frac{1}{\rho_m A_{m1} v_r}, \quad (45)$$

where A_{mi1} is the cross section of a particle in case $l = 1$ and ρ_m is the number density of these particles. The relative velocity is approximated for simplicity by the velocity caused by turbulence, $v_r = v_{\text{turb}}$, and is assumed to be independent of the particle size and filling factor.

In Nomura & Nakagawa (2006), coagulation is balanced by the radial drift of the particles with a velocity

$$v_d = g_d \tau_f, \quad (46)$$

where g_d is the local acceleration caused by the sub-Keplerian motion of the particle due to gas drag. The friction time of a given particle is

$$\tau_f = \frac{2}{9} \frac{\rho_p}{\rho_g} \frac{r_d^2}{v_m}, \quad (47)$$

with ρ_p, ρ_g, r_d, and v_m being the mass density of the dust particle (proportional to l), the mass density of the gas, the maximum radius particles can grow, and the mean molecular velocity of the gas, respectively (see Weidenschilling 1977). Here, ρ_p depends on the bulk density ρ_b of the dust monomers and the filling factor of the dust aggregate through

$$\rho_p = l \rho_b. \quad (48)$$

The drift timescale is given by

$$\tau_d = \frac{S_D}{v_d}, \quad (49)$$

where S_D is an arbitrary drift length. As the only dependency of Equations (49), (47), and (49) on the volume filling factor l is in ρ_p, τ_d is thus proportional to l^{-1}. This means that the coagulation timescale scales with $l^{\frac{2}{3}}$, whereas the drift timescale scales with l^{-1}.

To use the results of Nomura & Nakagawa (2006), a new maximum particle radius r_d (dependent on l) has to be found with which coagulation and radial drift still balance each other. The ratio of the two timescales,

$$\frac{\tau_k(l)}{\tau_d(l)} = \frac{2 l^{\frac{5}{3}} g_d \rho_b r_d^2}{9 \rho_m A_{m1} v_{\text{turb}} \rho_g v_m S_d}, \quad (50)$$

is proportional to $l^{\frac{5}{3}}$ and r_d^2. This means that the coagulation with a filling factor of l is still balanced by the radial drift if r_d is multiplied by a factor $l^{-\frac{5}{6}}$. Therefore, the maximum particle radius at 1 AU for a volume filling factor of $l = 0.40$ is about 0.5 m. From these considerations, it follows that the results of Nomura & Nakagawa (2006) are still valid for our lower filling factors if the maximum size of their particles is increased by a factor $l^{-\frac{5}{6}}$. The original coagulation timescale will then be changed by $l^{-\frac{2}{3}}$. However, the relative size distribution derived by Nomura & Nakagawa (2006) will remain unchanged. The original coagulation timescales are found in Nomura & Nakagawa (2006, their Figure 5), which is the time at which 70% of the total dust mass is in particles with a critical size at which they are lost from the coagulation process by fast radial drift. The dependency of the coagulation timescale on the disk radius is $\tau_k = 70$ years $\times l^{\frac{2}{3}}$ for $\alpha = 10^{-2}$ and $\tau_k = 500$ years $\times l^{\frac{2}{3}}$ for $\alpha = 10^{-4}$, respectively. We interpolated the timescales for the other radii assuming a power law. The resulting coagulation timescale as a function of the Kepler radius is shown in Figures 10 and 11 as solid lines in the top graph.

4.1.5. Timescale of Radial Turbulent Transport of Micrometer-sized Dust

The timescale of turbulent transport τ_{turb} of micrometer-sized dust is

$$\tau_{\text{turb}} = \frac{R^2}{v_{\text{turb}}}. \quad (51)$$

The turbulent gas viscosity is given by

$$\nu_{\text{turb}} = \alpha c_s H \tag{52}$$

(Shakura & Sunyaev 1973), with the sound speed

$$c_s = \sqrt{\frac{\gamma k_B T}{m_g}}, \tag{53}$$

where γ is the adiabatic exponent of H_2, k_B is Boltzmann's constant, and m_g is the mass of an H_2 gas molecule. The temperature is assumed to be dependent on the Kepler radius R_K via

$$T = 280\,\text{K} \left(\frac{R_K}{1\,\text{AU}}\right)^{-\frac{1}{2}} \tag{54}$$

(see Schräpler & Henning 2004). The timescale of turbulent particle transport as a function of the Kepler radius for $\alpha = 10^{-2}$ and $\alpha = 10^{-4}$ is shown in Figures 10 and 11, respectively (top graphs, dotted line). It is much longer than the coagulation and the erosion timescale. Therefore, the effect of turbulent particle transport is negligible for our considerations.

4.1.6. Particle Size Limit Caused by Radial Drift

The model of Nomura & Nakagawa (2006) is based on the assumption that *compact* particles that grow to a certain size are removed from the coagulation process by radial drift. Nomura & Nakagawa (2006) find in their Equation (24) and in the sentence below that these particles can grow close to the midplane to 32 cm, 80 cm, and 6 cm at 1 AU, 5.2 AU, and 30 AU, respectively for a turbulence strength of $\alpha = 10^{-2}$ and $\alpha = 10^{-4}$. The assumption of compact particles should now be dropped in favor of a realistic assessment of the porosity of the dust aggregates. We have seen above that fluffy dust aggregates get compacted by the continuous bombardment of micrometer-sized dust particles. Our model for the erosion efficiency (see Figure 8), which assumes a mean coordination number of 4, fits reasonably well. Such a coordination number is related to a volume filling factor by the relation shown in van de Lagemaat et al. (2001). From their Figure 4, we can conclude that the corresponding (surface) filling factor of the aggregates was increased to $l \approx 0.4$. We get a similar result for the (bulk) filling factor if we follow Zsom et al. (2010), who calculate that macroscopic dust aggregates should have volume filling factors $l \approx 0.4$, due to low-velocity bouncing collisions. Thus, we assume in the following a volume filling factor of $l = 0.4$ for large dust aggregates in protoplanetary disks. For this, we transformed the dust-aggregate sizes of Nomura & Nakagawa (2006) with the factor $l^{-\frac{5}{6}}$, calculated in Section 4.1.4. These transformed sizes are plotted as triangles in Figures 10 and 11 (lower graphs). In between the data points, we assumed power laws, which are shown as solid lines in the lower graphs of Figures 10 and 11.

4.1.7. Particle Size Limit Caused by Erosion

In Nomura & Nakagawa (2006), the coagulation of particles is limited due to the fact that large particles are lost by the drift toward the central star. However, in our case and at Kepler radii $R < 0.2$ AU ($\alpha = 10^{-2}$) and $R < 0.3$ AU ($\alpha = 10^{-4}$), the erosion timescale is much shorter than the coagulation timescale (see Figures 10 and 11, top graphs). Therefore, the particles can

only grow until the onset of erosion at drift velocities of 26 m s^{-1} (see Figure 8). The dependency of the impact velocity, v_{imp}, on the particle radius is estimated using Weidenschilling (1977, his Figure 3) for a particle density of 1000 kg m^{-3}. The impact velocity can be approximated by

$$v_{\text{imp}} = 26 \frac{\text{m}}{\text{s}} \left(\frac{r}{0.21\,\text{m}}\right)^{\frac{7}{5}}. \tag{55}$$

The dependency of the impact velocity, v_{imp}, on the Kepler radius is estimated using Weidenschilling (1977, his Figure 5). We have to cover a particle range from 0.08 m to 0.2 m of our dust aggregates with a volume filling factor of 0.4. As Weidenschilling (1977) assumed *compact* particles, we interpolated the curves in his Figure 5 with our filling factor of $l = 0.4$, keeping in mind that the independent variable is the friction time of the dust aggregates. Therefore, we used his 10 cm curve and approximate it with

$$v_{\text{imp}} = 26\,(\text{ms}^{-1}) \left(\frac{R(\text{AU})}{1.1\,\text{AU}}\right)^{-\frac{3}{5}}. \tag{56}$$

To find the particle radius for a given Kepler radius at which the drift velocity exceeds 26 m s^{-1} and therefore causes erosion, we combine Equations (55) and (56) to

$$v_{\text{imp}} = 26\,(\text{ms}^{-1}) \left(\frac{R(\text{AU})}{1.1\,\text{AU}}\right)^{-\frac{3}{5}} \left(\frac{r(\text{m})}{0.21\,\text{m}}\right)^{\frac{7}{5}}, \tag{57}$$

set v_{imp} to 26 m s^{-1}, and achieve

$$r = 0.21\text{m} \left(\frac{R(\text{AU})}{1.1\,\text{AU}}\right)^{\frac{3}{7}}. \tag{58}$$

Equation (58) is given as a dash-dotted line in the lower graphs of Figures 10 and 11. The particles size above would be reduced further in case the impact velocity driven by turbulence which is neglected here would be taken into account.

4.1.8. Number Density of Micrometer-sized Particles

At Kepler radii larger than 0.2 AU (for $\alpha = 10^{-2}$) and 0.3 AU (for $\alpha = 10^{-4}$), the timescale of the erosion is much larger than the coagulation timescale (see top graph in Figures 10 and 11). This means that particles can grow to the size predicted in Section 4.1.4 and the number density of the micrometer-sized particles is given by Equation (32). For Kepler radii smaller than the above values, the timescale for the erosion of large particles is much shorter than the coagulation timescale. This means that particles can only grow as long as their relative motion to the gas is smaller than the threshold at which the erosion process sets in. To calculate the number density of micrometer-sized dust particles produced by the erosion process at Kepler radii lower than given above, it is assumed that for all particles, which coagulate to a size where the relative motion to the gas causes erosion, the further coagulation is compensated by erosion. To get the number density of micrometer-sized particles, the production by erosion has to be balanced by their re-coagulation.

In the following, ρ_{00} denotes the total number density at a given Kepler radius if all the dust mass of the disk was in micrometer-sized particles and τ_{co} is the coagulation timescale to the particle size, r_{max}, at which erosion sets in. We assumed for simplicity that this is the same rate as the coagulation

to decimeter-sized particles given in Nomura & Nakagawa (2006, their Figure 5). However, coagulation continues, but all the mass gain of such dust aggregates caused by coagulation is immediately eroded away in regions where the erosional timescale is faster than the coagulation timescale. Thus, we get as the source term for monomer dust grains

$$\frac{d\rho_p}{dt} = \frac{\rho_{00}}{\tau_{co}}, \quad (59)$$

which gives the production rate of micrometer-sized dust particles by erosion. This rate is balanced by the coagulation of the micrometer-sized particles into dimers, i.e.,

$$\frac{d\rho_p}{dt} = -\frac{\sigma v_B \rho_p^2}{\sqrt{2}}, \quad (60)$$

where Equation (25) was used to integrate the coagulation, which takes place over the whole disk height. Combining Equations (59) and (60) leads to the stationary solution

$$\rho_{ps} = \sqrt{\frac{\rho_{00}\sqrt{2}}{\tau_{co}\sigma v_B}}. \quad (61)$$

The number density of the micrometer-sized dust particles, resulting from erosion (source term) and coagulation (sink term), is shown in Figure 10 for $\alpha = 10^{-2}$ and in Figure 11 for $\alpha = 10^{-4}$ (second graphs), as a function of distance to the central star, respectively. Here, the solid line shows the region in which the erosion timescales is larger than the coagulation timescale and the dash-dotted line shows where the erosion timescale is smaller than the coagulation timescale (see top graphs). We integrated all micrometer-sized dust particles over the entire disk volume and got for their total mass 1.7×10^{24} kg for $\alpha = 10^{-2}$ and 1.1×10^{24} kg for $\alpha = 10^{-4}$, respectively. Applying a minimum disk mass of $0.0425\,M_\odot$ for the gas mass and a total-mass ratio between dust and gas of 0.01, we get a mass fraction of the micrometer-sized dust particles with respect to the total dust mass in the disk of 2.0×10^{-3} for $\alpha = 10^{-2}$ and 1.3×10^{-3} for $\alpha = 10^{-4}$, respectively.

4.2. Consequences for Protoplanetary Disks

Figures 10 and 11 (top graphs) show that the process of impact erosion takes place at orbital distances smaller than 5 AU. At orbital distances smaller than 0.2 AU (for $\alpha = 10^{-2}$) and 0.3 AU (for $\alpha = 10^{-4}$), the erosion timescale of the large dust aggregates becomes smaller than the coagulation timescales. Hence, the dust aggregates can only grow as long as their relative velocity to the gas (and, thus, to the small dust particles) is smaller than the threshold velocity for erosion. Dust aggregates, which grew to larger sizes at larger orbital distances, radially drift inward from the outer disk and are then eroded to that size. The latter effect is neglected in the following, because the number of particles that drift in from further out is smaller than the particles that are locally produced by coagulation in that area. In the second graphs of Figures 10 and 11, the steady-state number density of micrometer-sized particles that are produced by the above effects and removed by coagulation are shown. At orbital distances in between ~5 AU and 0.2 AU (for $\alpha = 10^{-2}$) and ~5 AU and 0.3 AU (for $\alpha = 10^{-4}$), the erosion does not considerably affect the size of the large agglomerates (but still produces many micrometer-sized dust grains). At orbital distances smaller than 0.2 AU (for

$\alpha = 10^{-2}$) and 0.3 AU (for $\alpha = 10^{-4}$), the erosion balances the growth of the large dust aggregates by coagulation. Therefore, the number density increase of micrometer-sized dust particles toward smaller disk radii is not as steep as further out in the disk, because the drift velocity is reduced due to the smaller size of the largest particles. Here, radial diffusion has been neglected because its timescale is very long (see dotted lines in the top graphs of Figures 10 and 11). In the bottom graphs of Figures 10 and 11, the consequences of the erosion on the radii of the largest dust aggregates are shown. Note that 70% of the total dust mass of the disk is concentrated in the largest particles (Nomura & Nakagawa 2006). At disk radii larger than 0.2 AU (for $\alpha = 10^{-2}$) and 0.3 AU (for $\alpha = 10^{-4}$), the radii of the particles are nearly unaffected by erosion. The growth of dust aggregates at these radii is only limited by the inward migration of the particles. At smaller disk radii, the growth of the large dust aggregates is limited by erosion, which means that their sizes are reduced to less than 60% (at 0.1 AU) of the size without erosion.

In summary, the process of collisional erosion leads to a number density of micrometer-sized dust particles of up to 10^7 m^{-3} and limits the maximum dust-aggregate size to ~0.1 m at orbital distances of 0.3 AU. The ratio of micrometer-sized particles to the total dust mass at a given Kepler radius is shown in the third graph of Figures 10 and 11 for $\alpha = 10^{-2}$ and $\alpha = 10^{-4}$, respectively. For a minimum-mass solar nebula model, we integrated over the whole disk volume and found a total-mass fraction of the micrometer-sized dust particles of 2.0×10^{-3} for $\alpha = 10^{-2}$ and 1.3×10^{-3} for a $\alpha = 10^{-4}$, respectively.

4.3. Comparison with Observational Data

To compare the amount of micrometer-sized particles found above with observational data, we use the work of Furlan et al. (2006). Typical observations of Furlan et al. (2006) show dust depletion factors of 100–1000 which means that in their observed disks, 10^{-2}–10^{-3} of the total dust mass still resides in micrometer-sized particles, whereas the remaining dust mass is hidden in large dust aggregates. It is noted that the disk models used for their data interpretation have a slightly shallower density slope with Kepler radius than in the minimum-mass disk used here, but we do not think that this has an important influence on the observed mass depletion factor. In our bimodal model, 2.0×10^{-3} and 1.3×10^{-3} of the total dust mass is in micrometer-sized dust particles for $\alpha = 10^{-2}$ and $\alpha = 10^{-4}$, respectively. Seventy percent of the total dust mass is contained in large dust aggregates with a filling factor of 40%. This reproduces the observations of Furlan et al. (2006) very well.

In case the disks are already evolved and their gas density in the midplane at 1 AU has dropped to 10^{-9} kg m^{-3}, which is 10^{-3} of the value of a disk of minimum mass with an interstellar dust-to-gas mass ratio, the drift velocities of five millimeter-sized dust aggregates (having a filling factor of 40%), corresponding to the drift velocities of 2.7 mm compact particles (see above), are larger than 26 m s^{-1} (see Weidenschilling 1977, his Figure 4) and enable erosion much more efficiently. In this case, no decimeter- or meter-sized dust aggregates are necessary to explain the production and existence of micrometer-sized dust grains. This could also explain the cutoff at millimeter-sized grains seen in many disks of Ricci et al. (2010). In our model, the micrometer-sized dust particles are produced at Kepler radii smaller than ~5 AU. Hence, our model predicts that the disk is depleted

of micrometer-sized dust particles at large Kepler radii while somewhat larger grains are still present.

4.4. Irregular Dust Particles

As noted above, we used in our experiments monodisperse SiO_2 spheres as simulated protoplanetary dust particles. In reality, protoplanetary dust consists of grains with all possible shapes and follows a size distribution. As we found in an earlier paper (Blum et al. 2006), the tensile strength of dust aggregates consisting of polydisperse irregular SiO_2 particles is about five times smaller than that of the particles we used in the experiment described in Sections 2 and 3. As we can assume that the particle-release energy is proportional to the tensile strength, the erosional threshold should therefore approximately occur at 0.5 times smaller velocities. This means that the erosional process should work with more realistic particles up to disk radii of about 10 AU (using the disk model by Schräpler & Henning 2004). Hence, erosion should be properly treated in all simulations in which large dust aggregates (exceeding ∼10 cm in size) play a role and for the entire range of terrestrial planet and the inner part of the giant-planet formation zone.

5. SUMMARY

In protoplanetary disks, realistic dust-growth models (e.g., Zsom et al. 2010), which do not use a dust-retention mechanism (Okuzumi 2009; Okuzumi et al. 2011a, 2011b), fail to explain the observed large amount of micrometer-sized particles (Dullemond & Dominik 2005). Because high relative velocities between meter-sized dust aggregates and micrometer-sized dust particles exist in protoplanetary disks, we experimentally investigated in a first step whether collisions at these relative velocities lead to an erosion of the meter-sized aggregates, which could, in turn, be a source of micrometer-sized dust particles. We found that, after an initial stage in which an impacting particle can erode up to 10 dust grains from the fluffy dust agglomerate, the agglomerate is surface-compacted and passivated against further erosion at velocities lower than 26 m s^{-1}. At higher velocities, the erosion is reduced to 10% of its initial strength. In a second step, we explained and confirmed the occurrence of impact-induced erosion with a numerical model. In a third step, we developed an analytical disk model and implemented the experimentally found erosive effect. This model shows that erosion is a strong source of micrometer-sized dust particles in protoplanetary disks. The steady-state solution of the model shows that the micrometer-sized dust particles encompass a fraction of 0.20% (for α of 10^{-2}) and 0.13% (for 10^{-4}) of the total dust mass in a disk if we assume that 70% of the disk mass is in the form of meter-sized dust aggregates with a filling factor of 40%. A further outcome of our model is that larger dust aggregates get eroded very fast at small Kepler radii, because they possess higher relative velocities to the micrometer-sized particles. As their relative velocities are also dependent on their size, their growth is limited by erosion to ∼0.1 m at orbital distances smaller than a few tenth of an AU. Finally, we used our analytical model to discuss the amount of micrometer-sized particles in the observational data of Furlan

et al. (2006). We can reproduce their outcome with our erosion model. Assuming that the observed disks are already evolved and their gas density has dropped to 10^{-3} of a disk of minimum mass, drift velocities of 5 mm sized dust aggregates (with 40% filling factor) are large enough to enable erosion. In this case, no decimeter- or meter-sized dust aggregates are necessary to explain the production and existence of micrometer-sized dust grains. The erosive radius loss of grains larger than 5 mm could also explain the cutoff at millimeter-sized grains seen in many disks of Ricci et al. (2010).

REFERENCES

Blum, J. 2004, in ASP Conf. Ser. 309, Astrophysics of Dust, ed. A. N. Witt, G. C. Clayton, & B. T. Draine (San Francisco, CA: ASP), 369
Blum, J., & Schräpler, R. 2004, Phys. Rev. Lett., 93, 115503
Blum, J., Schräpler, R., Davidsson, B. J. R., & Trigo-Rodríguez, J. M. 2006, ApJ, 652, 1768
Blum, J., & Wurm, G. 2000, Icarus, 143, 138
Blum, J., & Wurm, G. 2008, Annu. Rev. Astron. Astrophys.ARA&A, 46, 21
Brauer, F., Dullemond, C. P., & Henning, T. 2008, A&A, 480, 859
Chokshi, A., Tielens, A. G. G. M., & Hollenbach, D. 1993, ApJ, 407, 806
Ciesla, F. J. 2007, ApJ, 654, L159
Cuzzi, J. N., Dobrovolskis, A. R., & Champney, J. M. 1993, Icarus, 106, 102
Dominik, C., & Tielens, A. G. G. M. 1997, ApJ, 480, 647
Dullemond, C. P., & Dominik, C. 2005, A&A, 434, 971
Furlan, E., et al. 2006, ApJS, 165, 568
Gammie, C. F. 1996, ApJ, 457, 355
Güttler, C., Blum, J., Zsom, A., Ormel, C. W., & Dullemond, C. P. 2010, A&A, 513, A56
Konstandopoulos, A. G. 2000, Powder Technology., 109, 262
van de Lagemaat, J., Benkstein, K. D., & Frank, A. J. 2001, J. Phys. Chem. B, 105 (50), 12434
Nakagawa, Y., Nakazawa, K., & Hayashi, C. 1981, Icarus, 45, 517
Nakagawa, Y., Sekiya, M., & Hayashi, C. 1986, Icarus, 67, 375
Nomura, H., & Nakagawa, Y. 2006, ApJ, 640, 1099
Okuzumi, S. 2009, ApJ, 698, 1122
Okuzumi, S., Tanaka, H., Takeuchi, T., & Sakagami, M. 2011a, ApJ, 731, 95
Okuzumi, S., Tanaka, H., Takeuchi, T., & Sakagami, M. 2011b, ApJ, 731, 96
Poppe, T., Blum, J., & Henning, T. 2000a, ApJ, 533, 472
Poppe, T., Blum, J., & Henning, T. 2000b, ApJ, 533, 454
Poppe, T., & Schräpler, R. 2005, A&A, 438, 1
Ricci, L., Testi, L., Natta, A., Neri, R., Cabrit, S., & Herczeg, G. J. 2010, A&A, 512, A15
Schmitt, W., Henning, T., & Mucha, R. 1997, A&A, 325, 569
Schräpler, R., & Henning, T. 2004, ApJ, 614, 960
Shakura, N. I., & Sunyaev, R. A. 1973, A&A, 24, 337
Stepinski, T. F. 1999, in Lunar and Planetary Institute Conference Abstracts, Layered Accretion in the Solar Nebula, 30, 1205
Wada, K., Tanaka, H., Suyama, T., Kimura, H., & Yamamoto, T. 2008, ApJ, 677, 1296
Weidenschilling, S. J. 1977, MNRAS, 180, 57
Weidenschilling, S. J. 1980, Icarus, 44, 172
Weidenschilling, S. J. 1984, Icarus, 60, 553
Weidenschilling, S. J. 1988, in Meteorites and the Early Solar System, ed. J. F. Kerridge & M. S. Matthews (Tucson, AZ: Univ. Arizona Press), 348
Weidenschilling, S. J. 2006, Icarus, 181, 572
Weidenschilling, S. J., & Cuzzi, J. N. 1993, in Protostars and Planets III, ed. E. H. Levy & J. I. Lunine (Tucson, AZ: Univ. Arizona Press), 1031
Zsom, A., Ormel, C. W., Güttler, C., Blum, J., & Dullemond, C. P. 2010, A&A, 513, A57